7. Vorne M, Soini I, Lantto T, Paakkinen S. Technetium-99m-HMPAO-labeled leukokytes in detection of inflammatory lesions: comparison with gallium-67-citrate. J Nucl Med 1989;30:1332–1336.

8. Perkins PJ. Early gallium-67 abdominal imaging: pitfalls due to bowel activity. Am J Roentgenol 1981;136:1016–1017.

9. Datz FL. Abdominal abscess detection: gallium, ^{111}In-, and ^{99m}Tc-labeled leukocytes, and polyclonal and monoclonal antibodies. Semin Nucl Med 1996;26:51–64.

10. Ebright JR, Soin JS, Manoli RS. The gallium scan. Problems and misuse in examination of patients with suspected infection. Arch Intern Med 1982;142:246–254.

11. Seabold JE, Nepola JV, Conrad GR, et al. Detection of osteomyelitis at fracture nonunion sites: comparison of two scintigraphic methods. Am J Roentgenol 1989;152:1021–1027.

12. Bekerman C, Hoffer PB, Bitran JD. The role of gallium-67 in the clinical evaluation of cancer. Semin Nucl Med 1984;14:296–323.

13. Lange JMA, Boucher CAB, Hollak CEM, et al. Failure of zidovudine prophylaxis after accidental exposure to HIV-1. N Engl J Med 1990;322:1375–1377.

14. Rubin RH, Fischman AJ, Callahan RJ, et al. In-111-labeled nonspecific immunoglobulin scanning in the detection of focal infection. N Engl J Med 1989;321:935–940.

15. Serafini AN, Garty I, Vargas-Cuba R, et al. Clinical evaluation of a scintigraphic method for diagnosing inflammations/infections using indium-111-labeled nonspecific human IgG. J Nucl Med 1991;32:2227–2232.

16. Datz FL, Anderson CE, Ahluwalia R, et al. The efficacy of indium-111-polyclonal IgG for the detection of infection and inflammation. J Nucl Med 1994;35:74–83.

17. Khalkali I, Mena I, Rauh DA, Diggles LE, Pham HL, Mason GR. 111-Indium-DTPA-IgG lung imaging in patients with pulmonary and HIV infection. Chest 1995;107:1336–1341.

18. Oyen WJG, Claessens RAMJ, Raemaekers JMM, de Pauw BE, van der Meer JWM, Corstens FHM. Diagnosing infection in febrile granulocytopenic patients with indium-111 labeled human IgG. J Clin Oncol 1992;10:61–68.

19. Fritzberg AR, Abrams PL, Beaumier PL, et al. Specific and stable labeling of antibodies with technetium-99m with a diamide dithiolate chelating agent. Proc Natl Acad Sci USA 1988;85:4025–4029.

20. Hnatowich DJ, Mardirossian G, Rusckowski M, Fogarasi M, Virzi F, Winnard P Jr. Directly and indirectly technetium-99m-labeled antibodies: a comparison of in vitro and animal in vivo properties. J Nucl Med 1993;34:109–119.

21. Oyen WJG, Claessens RAMJ, van der Meer JWM, Corstens FHM. Biodistribution and kinetics of radiolabeled proteins in rats with focal infection. J Nucl Med 1992;33:388–394.

22. Abrams MJ, Juweid M, ten Kate CI, et al. Technetium-99m-human polyclonal IgG radiolabeled via the hydrazino nicotinamide derivative for imaging focal sites of infection in rats. J Nucl Med 1990;31:2022–2028.

23. Claessens RAMJ, Boerman OC, Koenders EB, Oyen WJG, van der Meer JWM, Corstens FHM. Technetium-99m labelled hydrazinonicotinamido human non-specific polyclonal immunoglobulin G for detection of infectious foci: a comparison with two

24. Nijhof MW, Oyen WJG, van Kampen A, Claessens RAMJ, van der Meer JWM, Corstens FHM. Evaluation of infections of the locomotor system with indium-111-labeled human IgG scintigraphy. J Nucl Med 1997;38:1300–1305.

25. Oyen WJG, Claessens RAMJ, van der Meer JWM, Corstens FHM. Detection of subacute infectious foci with indium-111-labeled autologous leukocytes and with indium-111-labeled human nonspecific immunoglobulin G: a prospective comparative study. J Nucl Med 1991;32:1854–1860.

26. Arka A, Aktolun C, Gooden C, Epenetos A, Papadimitriou A. Tc-99m-labeled nonspecific polyclonal human immunoglobulin G is taken up by malignant tumors. Clin Nucl Med 1994;19:708–712.

27. Fischman AJ, Rubin RH, Khaw BA, et al. Detection of acute inflammation with In-111 labeled nonspecific polyclonal IgG. Semin Nucl Med 1988;18:335–344.

28. Callahan RJ, Barrow SA, Abrams MJ, Rubin RH, Fischman AJ. Biodistribution and dosimetry of technetium-99m-hydrazino nicotinamide IgG: comparison with indium-111-DTPA-IgG. J Nucl Med 1996;37:843–846.

29. Corstens FHM, Oyen WJG, Becker WS. Radioimmunoconjugates in the detection of infection and inflammation. Semin Nucl Med 1993;23:148–164.

30. Claessens RAMJ, Koenders EB, Oyen WJG, Corstens FHM. Retention of technetium-99m in infectious foci in rats after release from technetium-99m labelled human non-specific polyclonal immunoglobulin G: a dual study with hydrazinonicotinamido and iminothiolano immunoglobulin. Eur J Nucl Med 1996;23:1536–1539.

31. Goedemans WT, Panek KJ. A new method for labeling with ^{99m}Tc [Abstract]. J Nucl Med Allied Sci 1989;33:286.

32. Hovi I, Taavitsainen M, Lantto T, Vorne M, Paul R, Remes K. Technetium-99m-HMPAO-labeled leukocytes and technetium-99m-labeled human polyclonal immunoglobulin G in diagnosis of focal purulent disease. J Nucl Med 1993;34:1428–1434.

33. Buscombe JR, Lui D, Ensing G, de Jong R, Ell PJ. ^{99m}Tc-human immunoglobulin (HIG): first results of a new agent for the localization of infection and inflammation. Eur J Nucl Med 1990;16:649–655.

34. Moretti JL, Rapin JR, Saccavini JC, Lageron A, Le Poncin M, Bardy A. 2,3-Dimercaptosuccinic acid chelates: their structure and biological behaviour. In: Raynaud C, ed. Proceedings of the Third World Congress of Nuclear Medicine and Biology. Paris: Nuclear Medicine and Biology; 1982:1651–1654.

35. Spinelli F, Milella M, Sara R, Banfi F, Possa M, Vigorelli R. The value of Tc-99m-labelled human immunoglobulin scan in the evaluation of Crohn's disease. Nucl Med 1990;27:274–278.

36. Arndt JW, van der Sluys-Veer A, Blok D, et al. A prospective comparison of Tc-99m-labeled polyclonal human immunoglobulin and In-111 granulocytes for localization of inflammatory bowel disease. Acta Radiol 1992;33:140–144.

37. Larsen SK, Caldwell G, Higgins III JD, Abrams MJ, Solomon HF. Technetium complex of tricine: useful precursor for the ^{99m}Tc-labelling of hydrazino nicotinamide modified proteins [Abstract]. J Labelled Compd Rad 1994;35:1–2.

Iterative Reconstruction of Fluorine-18 SPECT Using Geometric Point Response Correction

Gengsheng L. Zeng, Grant T. Gullberg, Chuanyong Bai, Paul E. Christian, Frederick Trisjono, Edward V.R. Di Bella, Jared W. Tanner and Hugh T. Morgan

University of Utah, Salt Lake City, Utah; and Picker International, Inc., Cleveland, Ohio

This article demonstrates resolution recovery in ^{18}F SPECT image reconstruction by using an iterative algorithm that corrects for the system geometric response. **Methods:** Patient and phantom studies were performed using a Picker PRISM 3000 three-detector SPECT system (Picker International, Inc., Cleveland, OH) to image ^{18}F with 511 keV collimators. A measured point response function of the imaging system was used in an iterative reconstruction algorithm in which the projector and backprojector modeled the system point response function by using an efficient layer-by-layer blurring technique. The blurring function was a five-element kernel in the shape of a cross. The iterative reconstruction algorithm was an ordered-subset maximum-likelihood expectation maximization algorithm. **Results:** The iterative reconstruction algorithm with geometric response correction showed an improvement in resolution over the filtered backprojection reconstruction and the iterative reconstruction without correction. **Conclusion:** The proposed iterative reconstruction algorithm with geometric response correction is efficient and effective with significant resolution recovery.

Recent efforts have used SPECT systems for imaging positron emitters such as ^{18}F. The reason has been that ^{18}F-FDG is so effective in imaging metabolism that it gives high-contrast images between viable and nonviable tissue and between malignant and benign tissue. The problem with SPECT imaging of 511 keV photons is low sensitivity due to poor geometric efficiency and poor crystal sensitivity and poor resolution due to the need for thick septum and large holes in 511 keV collimators. It is hypothesized that by modeling the spatially varying geometric response of these collimators the resolution of reconstructed SPECT images can be improved, and it may be comparable to results obtained with lower energy radiopharmaceuticals commonly used in clinical nuclear medicine.

Imaging with radioactive fluorine was first performed more than 30 yr ago. In 1962, Blau et al. (1) used a small scintillation probe to acquire images of the uptake of ^{18}F in bone. In 1965,

Anger et al. used a positron camera (2) to perform ^{18}F bone scans (3). The first peer-reviewed article on the use of ^{18}F-FDG in humans was published in 1979 (4). Metabolic imaging with ^{18}F-FDG has played an increasing role over the years in oncology and cardiology (5,6). Most of this imaging was performed using PET before the recent resurgence of the use of SPECT in cardiac viability studies (7–9). Even though PET outperforms SPECT in terms of sensitivity and resolution, while imaging positron emissions, SPECT is able to image multiple agents simultaneously. Another advantage of using a SPECT system is its low cost and wider availability.

This article describes a method that efficiently models the spatially varying geometric response of 511 keV collimators in the projection and backprojection operations of an iterative reconstruction algorithm. The iterative algorithm is an ordered-subset maximum-likelihood (OS-ML) expectation maximization algorithm. It is applied to SPECT data collected from patient brain and heart studies that use ^{18}F-FDG and from phantom studies that use ^{18}F. The algorithm performed a geometric point response correction, no correction for attenuation or scatter was implemented.

MATERIALS AND METHODS

SPECT Imaging System

A three-detector Picker PRISM 3000 (Picker International, Inc., Cleveland, OH) with ultrahigh-energy parallel-hole collimators was used in the ^{18}F studies. The detailed collimator specification, including sensitivity/resolution measurements, can be found in an article by Leichner et al. (10). The collimators had hexagonal holes with a flat-side-to-flat-side diameter of 5.08 mm, septal thickness of 3.43 mm and holes of 77.0 mm length. The full-width at the half maximum (FWHM) at 200 mm (source-to-collimator distance) was 23 mm and at 100 mm was 17 mm as measured by a point source.

Reconstruction Algorithm

The maximum likelihood-expectation maximization (ML-EM) algorithm is a reconstruction method commonly used in SPECT because of its unique properties of non-negativity and proper Poisson noise modeling (11). This algorithm has been used to compensate for imaging physics such as attenuation, system point spread function and scatter (12–16). The ML-EM algorithm can be expressed as:

$$x_i^{(new)} = \frac{x_i^{(old)}}{\sum\limits_j c_{ij}} \sum\limits_j \frac{c_{ij}P_j}{\sum\limits_k c_{kj}x_k^{(old)}}, \qquad \text{Eq. 1}$$

where x_i is the ith voxel in the image volume, P_j is the jth projection bin (indexing the location on the detector and the view angle of the detector) and c_{ij} is the factor that the ith voxel contributes to the jth projection bin. The summation over k is referred to as a projector, and the summation over j is called a backprojector. In this article, a rotation (14), layer-by-layer blurring projector/backprojector (17–19) was chosen.

The algorithm in Equation 1 can be implemented as an ordered-subset version (20,27). The whole set of indices j is divided into subsets, and at each image update the index j goes through only one subset. One iteration is defined as when all the subsets have been visited once. Using an ordered-subset algorithm speeds up convergence. The ordered-subset in our implementation consisted of four views, which were 90° apart from each other. However, it has not been proven that an ordered-subset algorithm would necessarily converge.

Blurring Function Modeling

At each projection view, the image volume was rotated so that the face of the image volume was parallel to the detector as shown in Figure 1A. The rotation was achieved by a three-pass shear method with linear interpolation (21,22). For each layer parallel to
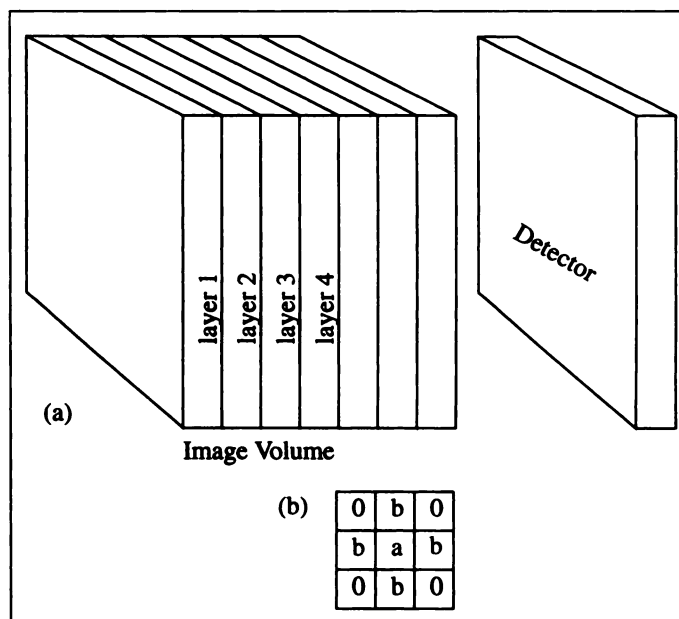

FIGURE 1. (A) The image volume is rotated to face the detector at each projection view. (B) A five-point convolution kernel is calculated for each layer.

the detector, a two-dimensional, five-point cross convolution kernel (17) was calculated according to details given in the Appendix. The incremental blurring was realized as follows: First the farthest layer from the detector (layer one in Fig. 1A) was convolved with its corresponding five-point cross convolution kernel (Fig. 1B), and the resultant two-dimensional image was added to layer two. Then, the updated layer two was convolved with its corresponding five-point cross kernel and added to layer three. This was repeated until the plane nearest the detector was reached.

Details for calculating the five-point cross kernels are given in the Appendix. A linear relation (23) between the FWHM of the point source image and the distance from the point source to the detector was determined by fitting the multiple point response function measurements at different distances. After extracting the dimension of the ^{18}F source, the resultant relation was:

$$FWHM(d) = 0.067d + 1.43, \qquad \text{Eq. 2}$$

where the units of distance d and FWHM are both mm. This relation was used to calculate the five-point kernels that were used in all patient and phantom studies. Our collimator had hexagonal holes. Thus, its point-spread function was not exactly two-dimensional symmetric. Both line source and point source measurements at different distances showed that the differences between the FWHM in the horizontal and vertical directions were within 2.5%. Therefore, it was reasonable to approximate the point response as a two-dimensional symmetric function.

Physical Hoffman Brain Phantom Studies

A shipment of ^{18}F was flown from Syncor (Phoenix, Arizona) to Salt Lake City for the phantom studies. The Hoffman brain phantom (Data Spectrum Corp., Hillsborough, NC) was filled with 296 MBq (8 mCi) of ^{18}F 8 min before scanning. The imaging window was 15% centered at 511 keV. A continuous gantry motion was used with a total scanning time of 20 min. The distance from the center of rotation to the detector plane was 23 cm; the center of rotation to the collimator was 14 cm. The projections were acquired at 120 angles over 360° in 64 × 64 arrays with a pixel size of 3.56 mm. Five iterations of the OS-ML algorithm was used in the reconstruction.
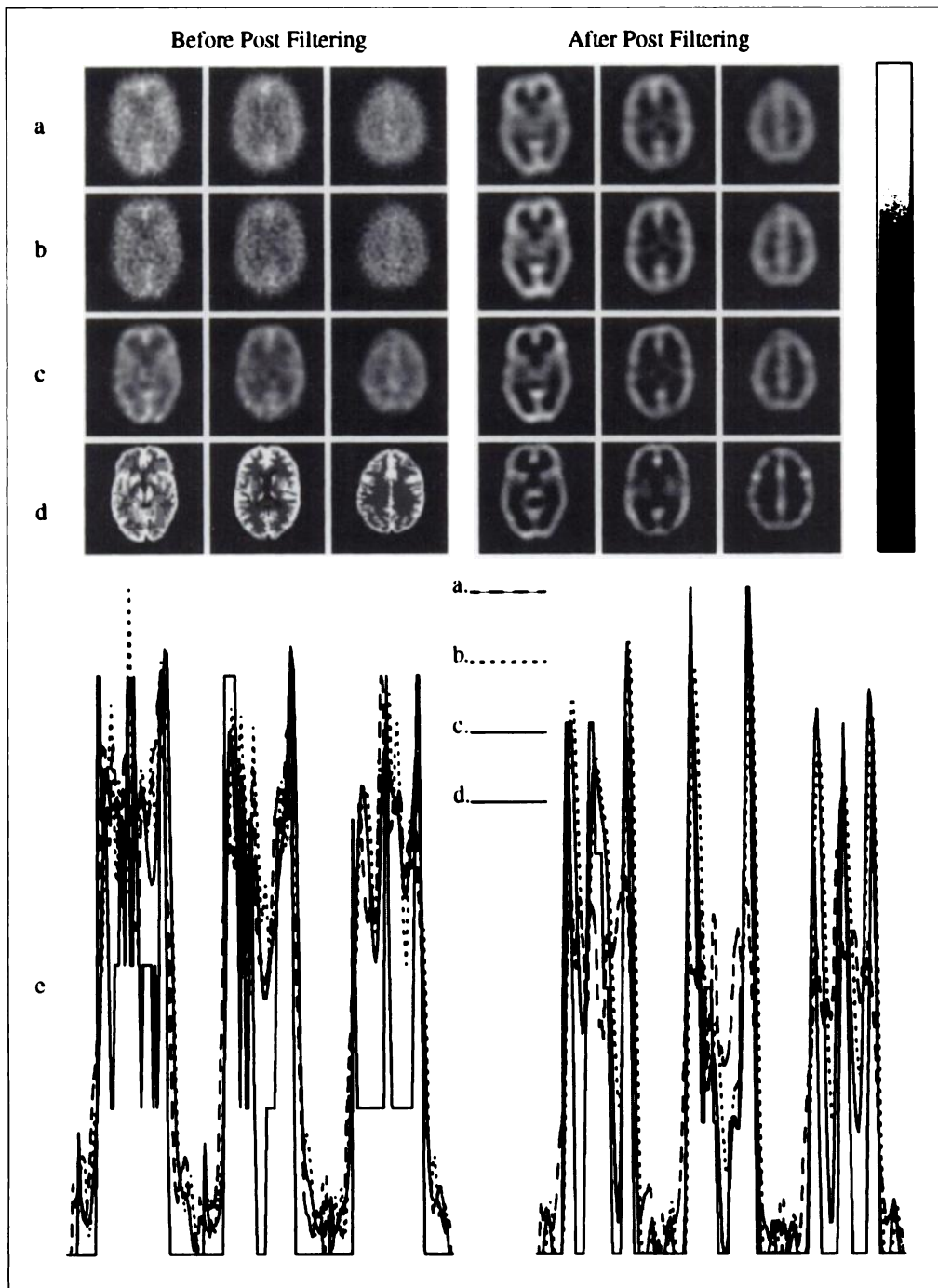
FIGURE 2. Reconstructions of [18]F Hoffman brain phantom data using the FBP (A), the OS-ML (B) without point response correction after five iterations and the OS-ML (C) with point response correction after five iterations. Ideal bit-map representation (D). Profiles along central horizontal lines (E).

Patient Brain Study

The data for the patient brain study were acquired at the University of Nebraska Medical Center using a Picker PRISM 3000 SPECT system. The patient (female, 53-yr-old) was injected with 370 MBq (10 mCi) of ^{18}F FDG 9 min before scanning. The imaging window was 15% centered at 511 keV. The gantry motion was step-and-shoot. A circular scanning orbit was used, and the detector radius was 25.61 cm. The projections from the three detectors were acquired at 120 angles over 360°. There were 40 stops with 60 sec at each stop giving a total scanning time of 44 min. The projection data were stored in 120 64 × 64 arrays with a pixel size of 7.12 mm in both horizontal and vertical directions. All the iterative reconstructions used five iterations.

Patient Cardiac Study

The data for the patient cardiac study were acquired at the AZR Dijkzigt Hospital in Rotterdam, The Netherlands, with a Picker PRISM 3000 SPECT system. The patient (male, 73-yr-old) was injected with 222 MBq (6 mCi) of ^{18}F FDG 3 min before scanning. The imaging window was 15% centered at 511 keV. A noncircular scanning orbit was used with a detector radius of approximately 30 cm. The gantry motion was continuous with a total scanning time of 33 min. The projections were acquired at 120 angles over 360° into 64 × 64 arrays with a pixel size of 4.45 mm in both horizontal and vertical directions. Five iterations were used in all the iterative reconstructions.

RESULTS

Figures 2–4 show the transverse views of the reconstructions from the Hoffman brain phantom data, the patient brain data and the patient cardiac data, respectively. All three sets of images show the filtered backprojection reconstruction in A, the iterative reconstruction without system point response compen-
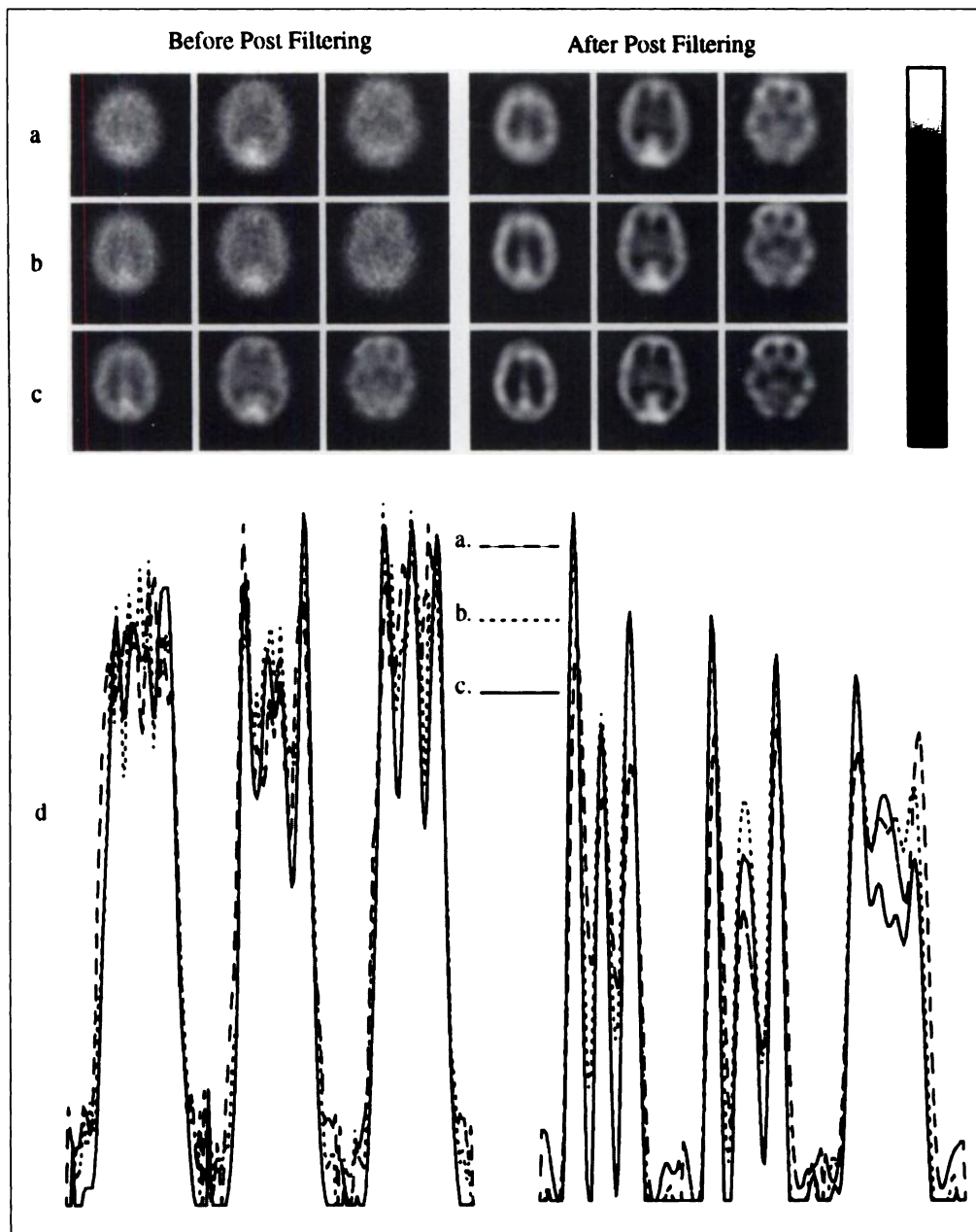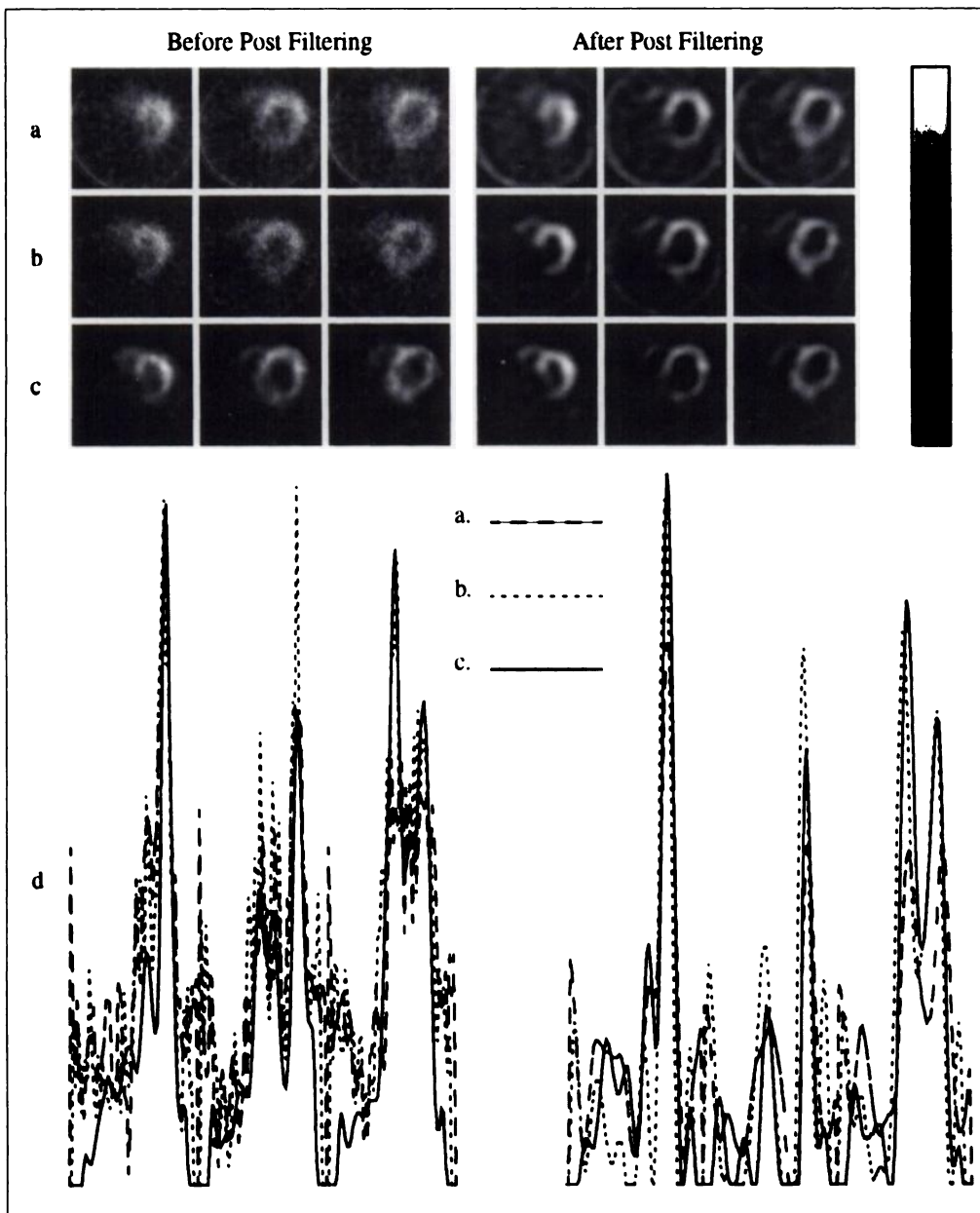
FIGURE 3. Reconstructions of ^{18}F-FDG patient brain data using the FBP (A), the OS-ML (B) without point response correction after E5 iterations and the OS-ML (C) with point response correction after five iterations. Profiles along the central horizontal lines (D).

sation in B and the iterative reconstruction with system point response compensation in C. The collimators had thick septa of 3.43 mm, and a black septal pattern could be clearly visualized in the projection data. To remove the pattern, all of the projections were first low-pass filtered before reconstruction as suggested in Leichner et al.'s article (10). The low-pass prefilter was an averaging filter. A 3 × 3 kernel was used, and its values were 1/9 for each cell in the kernel. Note that the point response measurements were also first low-pass filtered before they were used to estimate the system FWHM functions. A three-dimensional Metz postfilter (24) was applied to all the reconstructions on the left. The filtered images are shown on the right. To show the ideal images of the Hoffman brain phantom, a bit-map is shown in Figure 2D. The computation time for each slice (64 × 64) was 2 sec per iteration using one processor on a Sun Ultra Enterprise 3000 workstation (Milpitas, CA) (four processors at 167 MHz each).

DISCUSSION

FDG patient brain and heart SPECT studies and ^{18}F phantom SPECT studies were performed using Picker PRISM 3000 SPECT systems at various facilities with parallel-hole collimators specially designed for 511 keV. The iterative reconstructions with the OS-ML algorithm with system point response correction were compared with filtered backprojection reconstructions and iterative reconstruction without system point response correction. The projector and backprojector in the iterative reconstruction algorithm used a layer-by-layer incremental blurring scheme to model the distance-dependent collimator geometric point response function. On a Sun Ultra Enterprise 3000 workstation, the iterative algorithm required 2 sec per iteration for each (64 × 64) slice. The reconstructions from the iterative algorithm with collimator geometric point response correction showed improved resolution over the filtered backprojection results and iterative algorithm results without collimator geometric point response correction.

FIGURE 4. Reconstructions of ^{18}F-FDG patient cardiac data using the FBP (A), the OS-ML (B) without point response correction after five iterations and the OS-ML (C) with point response correction after five iterations. Profiles along the central horizontal lines (D).

A small 3 × 3 two-dimensional low-pass filter was applied to all projection data to remove the collimator hole pattern, as suggested in Leichner et al.'s article (*10*), and to remove some high-frequency noise. Because this prefiltering is linear and shift-invariant, it can be incorporated in the overall system point response function. Therefore, any resolution loss because of prefiltering can also be modeled during the iterative reconstruction procedure.

It is observed that the iterative reconstruction with geometric point response correction allows smoothing without loss of resolution. In this article, both the filtered backprojection algorithm and the iterative reconstruction algorithm used the same sets of slightly low-pass filtered projection data. However, the filtered backprojection and iterative reconstructions without corrections were much noisier than those obtained from the iterative reconstructions with depth-dependent point response correction. This is partially because the projector and back-projector that modeled the geometric point response inherently contained a blurring function that reduced the high-frequency noise. Of course, the high-frequency noise can also be suppressed by a linear three-dimensional postfilter (*24*). For exam-

ple, a three-dimensional post-Metz filter can improve the image quality significantly. A Metz filter suppresses the high-frequency noise and enhances the midfrequency components. However, some clinically important high-frequency details can also be suppressed by using a Metz filter. The reconstructions with depth-dependent point response correction produce improved resolution over that of the reconstructions without the correction.

The iterative algorithms used to correct for system point response have improved tremendously in computation time over the last few years. A ray-tracing projector/backprojector was originally implemented (*12*) that required 100 iterations of an EM-ML algorithm to obtain a result comparable to that obtained with five iterations of the OS-ML algorithm. Total reconstruction time for a 64 × 64 × 64 image array was 400 hr on an IBM 3090 computer (*12*). The algorithm was later made 50 times faster (total reconstruction time was 8 hr) by rotating the image as done currently and calculating the blurring for each layer by applying a full convolution kernel in the frequency domain, which modeled the effect of the point response function at that layer (*13*). The new proposed algorithm can

reconstruct a 64 × 64 × 64 image array with system point response correction in about 10 min on a Sun Ultra Enterprise 3000 workstation by using incremental small convolution kernels and only five iterations of the OS-ML algorithm, due to its fast convergent property.

It is observed in studying the feasibility of using SPECT to image ^{18}F-FDG that it is necessary to correct for the spatially varying geometric point response of the 511 keV collimators in order to obtain images comparable to those obtained with low energy radiopharmaceuticals commonly used in the clinic. The proposed reconstruction technique improves the contrast, which is expected to increase lesion detectability in clinical diagnosis. In addition, resolution recovery will be especially important for quantitative studies, such as those that use dynamic SPECT, where bias of kinetic parameters is significantly affected by resolution.

In iterative algorithms, each iteration can be treated as applying a spatially variant filter to the image. The resolution recovery varies for different frequency components and for different parts of the image. Their nonlinear nature makes the frequency response and noise propagation of iterative algorithms more difficult to study than in analytical alogrithms. Other researchers have made significant progress in using analytical algorithms to correct for depth-dependent blurring and uniform attenuation (25,26); however, these algorithms cannot handle nonuniform attenuation and scatter.

CONCLUSION

The proposed iterative reconstruction algorithm with geometric response correction is efficient and effective with significant resolution recovery. Post-filtering is not encouraged because it suppresses clinically important high-frequency details while suppressing noise.

APPENDIX

The five-point cross convolution kernels used in the incremental layer-by-layer blurring are derived. The kernels are approximated from Gaussian point spread functions, which are used to model the spatially varying point response of the 511 keV parallel collimators/camera system. For parallel collimators, the s.d. of these Gaussians is a linear function of the distance from the point source to the detector (23).

If two measurements of the FWHM, w_1 and w_2, are made at two distances, d_1 and d_2, respectively, the s.d. of the point spread function at distance d is (23):

$$\hat{\sigma}_d = \alpha d + \hat{\sigma}_0, \qquad \text{Eq. A1}$$

where

$$\alpha = \frac{(w_1 - w_2)/\sqrt{8 \ln 2}}{d_1 - d_2}, \qquad \text{Eq. A2}$$

and

$$\hat{\sigma}_0 = w_1/\sqrt{8 \ln 2} - d_1\alpha. \qquad \text{Eq. A3}$$

Here $1/\sqrt{8 \ln 2}$ is the conversion factor to convert a FWHM to a Gaussian s.d. For the 511 keV collimators used in this article, the linear function in Equation A1 was calculated by using $d_1 = 23$ cm, $w_1 = 1.84$ cm, $d_2 = 0$ cm and $w_2 = 0.38$ cm.

Incremental layer-by-layer blurring is implemented by a series of convolutions starting with the layer farthest from the detector:

$$\text{projection} = \{[(\text{layer}_1 * h_1 + \text{layer}_2) * h_2 + \text{layer}_3] *$$
$$h_3 + \text{layer}_4\} * h_5 + \dots, \qquad \text{Eq. A4}$$

where * denotes the two-dimensional convolution. Each h_k is a two-dimensional convolution kernel with a variance σ_k^2. If s is the

layer thickness, and if layer k is at a distance d, then the variance σ_k^2 is:

$$\sigma_k^2 = \hat{\sigma}_d^2 - \hat{\sigma}_{(d-s)}^2, \qquad \text{Eq. A5}$$

where $\hat{\sigma}_d^2$ is the variance of the Gaussian point spread function at the distance d, and $\hat{\sigma}_{(d-s)}^2$ is the variance of the Gaussian point spread function at the distance d-s away from the collimator. This follows from the fact that the convolution of two Gaussians is a Gaussian with a variance equal to the sum of the variances of each Gaussian. Using Equation A1, the expression for σ_k^2 in Equation A5 becomes:

$$\sigma_k^2 = d(2s\alpha^2) + (2s\alpha\hat{\sigma}_0 - \alpha^2 s^2). \qquad \text{Eq. A6}$$

This gives an expression for the variance of the convolution kernel h_k, which is the incremental blurring applied in summing layer k to layer k-1.

In the algorithm implementation, the convolution kernel h_k is approximated by a five-point cross-kernel of the following form:

0	b	0
b	a	b
0	b	0

Eq. A7

with the normalization constraint that the sum of the kernel entries is unity, yielding

$$b = \frac{1 - a}{4} \quad \text{for } 0 < a \leq 1. \qquad \text{Eq. A8}$$

Assume that the system point response function is Gaussian. Let

$$f_1(x, y) = \frac{1}{\sqrt{2\pi\sigma_1^2}} \exp\left(-\frac{x^2 + y^2}{2\sigma_1^2}\right) \qquad \text{Eq. A9}$$

be the point spread function at distance d and

$$f_2(x, y) = \frac{1}{\sqrt{2\pi\sigma_2^2}} \exp\left(-\frac{x^2 + y^2}{2\sigma_2^2}\right) \qquad \text{Eq. A10}$$

be the point spread function at distance d + s. If f_2 can be approximated by convolving f_1 with the kernel defined in Equation A7, then

$$f_2(x, y) \approx af_1(x, y) + b[f_1(x + 1, y) + f_1(x - 1, y) + f_1(x, y + 1)$$
$$+ f_1(x, y - 1)]. \qquad \text{Eq. A11}$$

Using Equations A8-A11 becomes

$$t_3 \approx at_1 + \frac{1 - a}{4} t_2, \qquad \text{Eq. A12}$$

where

$$t_1(x, y) = \exp\left(-\frac{x^2 + y^2}{2\sigma_1^2}\right), \qquad \text{Eq. A13}$$

$$t_2(x, y) = \exp\left(-\frac{(x + 1)^2 + y^2}{2\sigma_1^2}\right) + \exp\left(-\frac{(x - 1)^2 + y^2}{2\sigma_1^2}\right)$$
$$+ \exp\left(-\frac{x^2 + (y + 1)^2}{2\sigma_1^2}\right) + \exp\left(-\frac{x^2 + (y - 1)^2}{2\sigma_1^2}\right) \qquad \text{Eq. A14}$$

$$t_3(x, y) = \frac{\sigma_1}{\sigma_2} \exp\left(-\frac{x^2 + y^2}{2\sigma_1^2}\right). \qquad \text{Eq. A15}$$

To find the parameter a, it is necessary to minimize the following cost function F:

$$F(a) = \sum_x \sum_y \left[a\, t_1(x, y) + \frac{1 - a}{4} t_2(x, y) - t_3(x, y) \right]^2. \qquad \text{Eq. A16}$$

Setting the first derivative of F(a) to zero, parameter a is obtained as:

$$a = \frac{\sum_x \sum_y (t_3 - t_2/4)(t_1 - t_2/4)}{\sum_x \sum_y (t_1 - t_2/4)^2}. \qquad \text{Eq. A17}$$

Once parameter a is obtained, parameter b is calculated via Equation A8.

REFERENCES

1. Blau M, Nagler W, Bender MA. Fluorine-18: a new isotope for bone scanning. *J Nucl Med* 1962;3:332–334.
2. Anger HO, Van Dyke D, Gottschalk A, Yano Y, Schaer LR. The scintillation camera in diagnosis and research. *Nucleonics* 1965;23:57–62.
3. Van Dyke D, Anger HO, Yano Y, Bozzini C. Bone blood flow shown with F-18 and the positron camera. *Am J Physiol* 1965;209:65–70.
4. Reivich M, Kuhl D, Wolf A, et al. The [^{18}F]fluorodeoxyglucose method for measurement of local cerebral glucose utilization in man. *Circ Res* 1979;44:127–137.
5. Strauss LG, Conti PS. The applications of PET in clinical oncology. *J Nucl Med* 1991;32:623–648.
6. Coleman RE, Hoffman JM, Hanson MW, Sostman HD, Schold SC. Clinical application of PET for the evaluation of brain tumors. *J Nucl Med* 1991;32:616–622.
7. Burt RW, Perkins OW, Oppenheim BE, et al. Direct comparison of fluorine-18-FDG SPECT, fluorine-18-FDG PET and rest thallium-201 SPECT for detection of myocardial viability. *J Nucl Med* 1995;36:176–179.
8. Martin WH, Delbeke D, Patton JA, et al. FDG-SPECT: Correlation with FDG-PET. *J Nucl Med* 1995;36:988–995.
9. Delbeke D, Videlefsky S, Patton JA, et al. Rest myocardial perfusion/metabolism imaging using simultaneous dual-isotope acquisition SPECT with technetium-99m-MIBI/fluorine-18-FDG. *J Nucl Med* 1995;36:2110–2119.
10. Leichner PK, Morgan HT, Holdeman KP, et al. SPECT imaging of fluorine-18. *J Nucl Med* 1995;36:1472–1475.
11. Lange K, Carson R. EM reconstruction algorithms for emission and transmission tomography. *J Comput Assist Tomogr* 1984;8:306–316.
12. Zeng GL, Gullberg GT, Tsui BMW, Terry JA. Three-dimensional iterative reconstruction algorithms with attenuation and geometric point response correction. *IEEE Trans Nucl Sci* 1991;38:693–702.
13. Zeng GL, Gullberg GT. Frequency domain correction of the three-dimensional geometric point response function in SPECT imaging. *IEEE Trans Nucl Sci* 1992;39:1444–1453.
14. Liang Z, Jaszczak RJ, Turkington TG, Gilland DR, Coleman RE. Simultaneous compensation for attenuation, scatter and detector response of SPECT reconstruction in three dimensions. *Phys Med Biol* 1992:587–603.
15. Frey EC, Tsui BMW. A practical method for incorporating scatter in a projector-backprojector for accurate scatter compensation in SPECT. *IEEE Trans Nucl Sci* 1993;40:294–299.
16. Zeng GT, Hsieh YL, Gullberg GT. A rotating and warping projector-backprojector pair for fan-beam and cone-beam iterative algorithms. *IEEE Trans Nucl Sci* 1994;41:2807–2811.
17. Wallis JW, Miller TR, Miller MM, Hamill J. Rapid 3-D projection in iterative reconstruction using Gaussian diffusion [Abstract]. *J Nucl Med* 1996;37:63P.
18. McCarthy AW, Miller MI. Maximum likelihood SPECT in clinical computation times using mesh-connected parallel computers. *IEEE Trans Med Imag* 1991;10:426–436.
19. Di Bella EVR, Trisjono F, Zeng GL. Recursive blur models for SPECT depth-dependent response [Abstract]. *J Nucl Med* 1996;37:153P.
20. Hudson HM, Larkin RS. Accelerated EM reconstruction using ordered subsets of projection data. *IEEE Trans Med Imag* 1994;13:601–609.
21. Wolberg G. *Digital image warping*. Los Alamitos, CA: IEEE Computer Society Press; 1990.
22. Di Bella EVR, Barclay AB, Eisner RL, Schafer RW. A comparison of rotation-based methods for iterative reconstruction algorithm. *IEEE Trans Nucl Sci* 1996;43:3370–3376.
23. Metz CE, Atkins FB, Beck RN. The geometric transfer function component for scintillation camera collimators with straight parallel holes. *Phys Med Biol* 1980;25:1059–1070.
24. King MA, Glick SJ, Penney BC, Schwinger RB, Doherty PW. Interactive visual optimization of SPECT prereconstruction filtering. *J Nucl Med* 1987;28:1192–1198.
25. Hawkins WG, Yang NC, Leichner PK. Validation of the circular harmonic transform (CHT) algorithm for quantitative SPECT. *J Nucl Med* 1991;32:141–150.
26. Pan X, Metz CE, Chen CT. A class of analytical methods that compensate for attenuation and spatially-variant resolution in 2D SPECT. *IEEE Trans Nucl Sci* 1996;43:2244–2254.
27. Byrne CL. Block-iterative methods for image reconstruction from projections. *IEEE Trans Image Proc* 1996;5:792–794.

Pinhole SPECT Imaging in Normal and Morbid Ankles

Yong-Whee Bahk, Soo-Kyo Chung, Young-Ha Park, Sung-Hoon Kim and Hyoung-Koo Lee

Department of Radiology, Samsung Cheil Hospital, Seoul; and Department of Nuclear Medicine, Catholic University Medical College Hospitals, Seoul and Suwon, Korea

Pinhole SPECT can generate sectional nuclear images of a normal and morbid ankle and hindfoot with remarkably enhanced resolution by portraying the topography and pathological alterations in great detail. **Methods:** Pinhole SPECT was performed using a commercially available single-head, rotating gamma camera system by replacing the parallel-hole collimator used for planar SPECT with a pinhole collimator. The images were reconstructed in the same way as in planar SPECT by using the filtered back-projection algorithm and a Butterworth filter. First, we compared the scan resolution between the planar and pinhole SPECT images of a thyroid phantom and a normal ankle and hindfoot by working out pinhole SPECT anatomy with CT validation. Second, the clinical usefulness was assessed in one case each of fracture, reflex sympathetic dystrophy syndrome and rheumatoid arthritis of the ankle with radiographic correlation. The resolution of the pinhole SPECT and planar pinhole images was compared for these diseases. **Results:** The resolution of the pinhole SPECT of a thyroid phantom and of a normal ankle and hindfoot was significantly enhanced compared to the planar SPECT although image distortion was seen in the periphery of the field-of-view. The pinhole SPECT resolution was such that most of the anatomical landmarks were sharply delineated in the ankle and hindfoot and some useful diagnostic signs in the diseased ankle were visible. **Conclusion:** Pinhole SPECT can be performed using a single-head gamma camera system and filtered back-projection algorithm. It generates sectional scan images of both normal and morbid ankle and hindfoot with enhanced resolution portraying many anatomical landmarks and pathological signs in useful detail.

Key Words: SPECT; pinhole; bone; ankle

J Nucl Med 1998; 39:130–139